PAPER

Giant enhancement of coercivity in β -Ni(OH)₂ decorated Ti₃C₂T_x MXene nanosheets

To cite this article: Anup Debnath et al 2024 J. Phys. D: Appl. Phys. 57 355002

View the article online for updates and enhancements.

You may also like

- Synthesis of High Surface Area -Ni (OH) ₂ and Its Transformation into Nanosheets and Nanodisks by Hydrothermal <u>Treatment</u>

Go Sakai, Makoto Miyazaki and Tsuyoshi Kijima

- Synthesis of nanostructured -Ni(OH)₂ by electrochemical dissolution—precipitation and its application as a water oxidation catalyst

catalyst
Sang Cheol Jung, Soong Leong Sim, Ying
Woan Soon et al.

 Nickel hydroxide—carbon nanotube nanocomposites as supercapacitor electrodes: crystallinity dependent performances

Wenchao Jiang, Shengli Zhai, Li Wei et al.



Giant enhancement of coercivity in β -Ni(OH)₂ decorated Ti₃C₂T_x MXene nanosheets

Anup Debnath^{1,2}, Sumanta Bera¹, Gouranga Mahapatra¹, Arijit Kapuria¹ and Shyamal K Saha^{1,3,*}

E-mail: cnssks@iacs.res.in and sksaha@gs.ncku.edu.tw

Received 4 January 2024, revised 23 March 2024 Accepted for publication 29 May 2024 Published 6 June 2024



Abstract

Ti₃C₂T_r MXenes are of great interest due to their high conductivity, easy synthesis and unique functional properties. Functionalisation and structural engineering are essential for various applications because of their dramatic influences on different chemical and physical properties. Therefore, understanding the mechanism of the etching reaction of $Ti_3C_2T_r$ from its parent MAX phase is crucial. The structural details also need to be understood for application in different practical devices. In this study, 2D Ti₃C₂T_x sheets with an average thickness of 3.48 nm and lateral dimension of 5.5 μ m were synthesised by removing Al layers from the Ti₃AlC₂ MAX phase. The step-by-step etching mechanism was analysed with the help of Rietveld refinement of the powder x-ray diffraction data. The structural details and influence of different functional groups on the surface were also studied using transmission electron microscopy, x-ray photoelectron spectroscopy, and Raman spectroscopy. The magnetic behaviour and magnetic interaction of bare 2D $\text{Ti}_3\text{C}_2\text{T}_x$ decorated with β -Ni(OH)₂ nanosheets on its surface was studied. For the bare 2D Ti₃C₂T_x MXene sheets, a weak ferrimagnetic ordering with negligible coercivity was found. However, the β -Ni(OH)₂-decorated Ti₃C₂T_x MXene sheets exhibit strong ferrimagnetic ordering with a sufficiently large coercivity of 0.2 T at 2 K and a transition temperature of 246 K. The generation of this interfacial ferrimagnetism is discussed in light of the interfacial charge transfer originating from d-p mixing. These 2D magnets generated at the interface could be useful for application in different spintronic devices.

Supplementary material for this article is available online

Keywords: MXene, $Ti_3C_2T_x$, β -Ni(OH)₂, Rietveld refinement, charge-transfer, 2D ferrimagnet

1. Introduction

MXenes, a new kind of two-dimensional (2D) transition metal carbide or nitride with different functional groups, were

* Author to whom any correspondence should be addressed.

discovered in 2011 [1]. The general formula of the MXene is $M_{n+1}X_nT_x$, where n can have a value of 1–3. M represents an early transition metal atom such as Ti, V, Mo, Cr, etc and X represents the carbon and/or nitrogen atoms, whereas T_x represents different functional groups (such as -O, -OH, -F, -CI, -Br, -S, -NH, -Se, and -Te), which are attached to the surface terminations depending upon the reaction route

¹ School of Materials Sciences, Indian Association for the Cultivation of Science, 2A and 2B Raja S. C. Mullick Road, Jadavpur, Kolkata 700032, West Bengal, India

² Department of Physics, Jadavpur University, 188 Raja S. C. Mullick Road, Jadavpur, Kolkata 700032, West Bengal, India

³ Academy of Innovative Semiconductor and Sustainable Manufacturing, National Cheng Kung University, Tainan 701, Taiwan, R. O. C

[1]. Usually, MXenes are prepared by eliminating A-site elements from their parent MAX phases; A represents elements from group 13 or group 14 of the periodic table. In the MAX phases, A-site atoms (such as Al) are the most reactive sites and are bonded weakly compared to the M-X bond. This is why removing it from the MAX phase is relatively easier by selective etching reactions with different etchants. Ti₃C₂T_x was the first discovered and is the most studied 2D MXene. 2D Ti₃C₂T_r MXene is produced by removing Al-layers from the bulk Ti₃AlC₂ MAX phase using hydrofluoric acid (HF) at different concentrations or HF-containing or HF-forming compounds in a wet-chemical selective etching reaction. Since the discovery of 2D Ti₃C₂T_x, several articles related to different synthesis approaches and their multifunctional applications in various fields have been published [2–4]. 2D MXene sheets, especially 2D $Ti_3C_2T_x$, possess metallic behaviour with high conductivity ($\sim 2.4 \times 10^4 \text{ S} \cdot \text{cm}^{-1}$) and have attracted increased interest in the scientific community [5]. Because of its good electrical conductivity, surface properties, mechanical strength, and unique anisotropy, it has been used for potential applications in optical, flexible electronic, optoelectronic, energy, catalytic, and biomedical applications [6–12]. A step-by-step understanding of the synthesis mechanism and a detailed understanding of the crystal structure of the derived 2D Ti₃C₂T_x MXene materials from its parent Ti₃AlC₂ MAX phase are lacking. The literature also does not provide a thorough study of the magnetic behaviour of bare Ti₃C₂T_x crystals or their modification due to interfacial interactions with an antiferromagnet β -Ni(OH)₂. Theoretical research suggests that the nonbonding Ti d-orbital, positioned between the bonding (σ) and antibonding (σ^*) states of Ti-C and Ti-T_r bonds, probes the magnetic ordering in monolayer graphenelike $Ti_3C_2T_x$ [13]. Based on the spin polarisation, the numerical calculations suggest that the ground state of graphene-like $Ti_3C_2T_x$ has an antiferromagnetic nature. Here, each Ti_1 layer (the outer site Ti in $Ti_3C_2T_x$) provides ferromagnetic ordering with a moment of 0.74 μ_B per Ti atom, whereas the Ti₂ layer (the inner site Ti in $Ti_3C_2T_x$) provides a very small or negligible moment ($<0.05 \mu_B$ per Ti atom) [14]. These two layers of Ti₁ atoms in two opposite layers are coupled antiferromagnetically. In practice, due to the presence of different functional groups, there is a development of electronic density of states near the Fermi level and, hence, the generation of a weak ferromagnetic effect at the edges of the 2D $Ti_3C_2T_x$ MXene sheets [15, 16]. This ferromagnetic ordering, generated due to the presence of different functional groups (T_x) , surpasses the antiferromagnetic arrangement from the nonbonding Ti 3d orbitals [16]. However, different groups of researchers have described various magnetic ordering models for Ti₃C₂T_x materials, such as antiferromagnetic, ferromagnetic or paramagnetic [15–17]. Therefore, there is a debate about the origin and nature of the magnetic behaviour of 2D Ti₃C₂T_x MXenes, and a detailed study is needed to understand its magnetic behaviour further. The literature shows that the previously reported articles did not consider the whole range of inverse susceptibility (1/ χ vs. T) data. To overcome this discrepancy and explore this issue, the entire range (2-300 K) of the inverse susceptibility data was considered in this study. All the available models were tried to fit with the experimental data. The magnetic behaviour of 2D $Ti_3C_2T_x$ MXenes were evaluated based on the best fit of the data.

Furthermore, due to the presence of different functional groups, especially T_F, which have a highly negatively charged environment on the surface, 2D Ti₃C₂T_x MXene sheets can be used as effective substrates for fabricating 'charge-transferinduced' ferrimagnets [18, 19]. Charge-transfer-induced ferrimagnets are fabricated by growing an antiferromagnetic layer such as β -Ni(OH)₂, β -Co(OH)₂, α -Fe₂O₃, etc, on a 2D substrate to share its charge with the antiferromagnetic layer at the interface, resulting in an imbalance in the antiferromagnetic ordering. An imbalance in the antiferromagnetic arrangement at the interface produces a net magnetic moment with a strong surface pinning effect [20]. Strong ordering of such moments produces a 2D ferrimagnet or ferromagnet with good coercivity [18, 21]. However, the main drawback of this kind of magnetism is the lower transition temperature (<200 K); hence, this material is unsuitable for practical applications.

In this article, the step-by-step etching of Al from the Ti₃AlC₂ MAX phase by HF-forming agents (LiF + HCl) to form the 2D $Ti_3C_2T_x$ MXene was studied. Here, Rietveld refinement was used to understand the step-by-step removal of Al layers from the MAX phase before they were ultimately converted into 2D MXenes. Because of the presence of different functional groups (T_x) on the surface of the 2D Ti₃C₂T_x MXene sheets, the crystal structure was strongly influenced. This result differs from the theoretically simulated actual crystal structure of Ti₃C₂ MXene. Hence, the refinement of the experimentally obtained powder x-ray diffraction data becomes much more complex. This study also determined the crystal structure (structural and microstructural details) of chemically synthesised 2D $Ti_3C_2T_x$ MXene sheets via Rietveld refinement. A decrease in the in-plane lattice parameters, i.e. a and b, and an increase in the out-of-plane lattice parameter, i.e. c, from their theoretically calculated values for the pure Ti₃C₂ MXene phase were observed. The maximum interlayer spacing for the β -Ni(OH)₂-decorated 2D Ti₃C₂T_x MXene sheets was found notably higher compared to their parent MAX phase. Thus, the as-synthesised 2D Ti₃C₂T_x MXene sheets become more suitable for different applications. In this study, ultrathin (approximately three-layered) 2D Ti₃C₂T_x MXene sheets with a uniform thickness was synthesised. The magnetic behaviour of chemically synthesised 2D Ti₃C₂T_r MXene sheets was investigated. The interfacial interaction of 2D Ti₃C₂T_x MXene sheets with as-grown antiferromagnetic β -Ni(OH)₂ layers on it was also studied. There are two polymorphs of Ni(OH)₂: the α -phase and the β -phase. The α -Ni(OH)₂ exhibits ferromagnetic behaviour, whereas the β-Ni(OH)₂ phase displays antiferromagnetic characteristics with a Neel temperature of approximately 26 K [21]. Notably, compared to conventional antiferromagnetic layers such as β -Co(OH)₂ and α -Fe₂O₃, β -Ni(OH)₂ demonstrates superior interfacial-interaction with various 2D template materials (e.g. rGO, MoS₂) during growth. Additionally, β -Ni(OH)₂ exhibits a higher coercivity value for the interfacial 2D magnetism induced by charge transfer, surpassing other antiferromagnetic layers [18–21]. In this study, the magnetic interaction between β -Ni(OH)₂ and 2D Ti₃C₂T_x micro-sheets was investigated, exploring the generation of an interfacial 2D ferrimagnet induced by charge-transfer. The interfacial magnetic interaction was also studied in this work.

2. Experimental section

2.1. Chemicals used

For the synthesis of the samples, titanium aluminium carbide powder [MAX (Ti₃AlC₂)] (Product no. NRE-58013, CAS No. 196506-01-1, Molecular weight $194.60 \text{ g mol}^{-1}$, Purity 99.9%, Nano Research Elements, India), lithium fluoride [LiF] (Product no. 04440, CAS No. 7789-24-4, Molecular weight 25.94 g mol⁻¹, Density 2.64 g cm⁻³ (25 °C), Purity 98%, Loba Chemie Pvt. Ltd, India), nickel (II) acetate tetrahydrate [Ni(OCOCH₃)₂,4H₂O] (Product no. 244 066, CAS No. 6018-89-9, Molecular weight $148.84 \text{ g mol}^{-1}$, Density 1.798 g cm⁻³ (25 °C), Purity 98%, Merck, India), hydrochloric acid (Product no. 100317, CAS No. 7647-01-0, Molecular weight 36.46 g mol⁻¹, Density 1.19 g cm⁻³ (20 °C), Purity 37%–38%, Merck, India), ammonium hydroxide solution [NH₄OH] (Product no. 221228, CAS No. 1336-21-6, Molecular weight 35.05 g mol⁻¹, Density 0.9 g cm⁻³ (25 °C), Purity 28%–30% NH₃ basis, Merck, India), ethanol [C₂H₅OH] (Product no. 100983, CAS No. 64-17-5, Molecular weight 46.07 g mol⁻¹, Density 0.79 g cm⁻³ (20 °C), Purity 99.9%, Merck, India), acetone [CH₃COCH₃] (Product no. 100014, CAS No. 67-64-1, Molecular weight 58.08 g mol⁻¹, Density 0.79 g cm⁻³ (20 °C), Purity 99.8%, Merck, India), and N,N-dimethylformamide (DMF) [HCON(CH₃)₂] (Product no. 103053, CAS No. 68-12-2, Molecular weight 73.09 g mol⁻¹, Density 0.944 g cm⁻³ (25 °C), Purity 99.8%, Merck, India) were purchased. All the reagents were used as received, and no further purification was performed.

2.2. Synthesis of $Ti_3C_2T_x$ MXene nanosheets

Several methods are available in the literature for synthesising Ti₃C₂T_x MXene sheets from the bulk Ti₃AlC₂ MAX phase. The crystallinity, sheet-thickness, lateral dimension and presence of different functional groups on the surface of synthesised Ti₃C₂T_x MXenes are entirely dependent upon the synthesis technique and post-synthesis treatment. Here, a modified method was used, reported elsewhere, to synthesise 2D Ti₃C₂T_x MXene sheets by wet-chemical etching of the parent MAX (Ti₃AlC₂) phase [2]. The synthesis procedure is demonstrated in figure 1. First, 4 ml of water in a plastic beaker was taken and added 12 ml of HCl. The mixture was stirred for 5 min to obtain a uniform solution. Then, 1 g of LiF was added to the previously prepared acid solution under stirring conditions. The reaction between HCl and LiF produces HF and LiCl. The reaction mechanism is as follows.

$$LiF + HCl \rightarrow HF + LiCl$$
 (1)

Then, 0.5 g of the MAX (Ti_3AlC_2) phase was slowly added to avoid generating excess heat. Ti_3AlC_2 reacts with a mixture of LiF and HCl to produce Ti_3C_2 with different functional groups (T_x) terminating its surface. The reaction mechanism is as follows

2 Ti₃AlC₂ + 6 LiF + 6 HCl
$$\rightarrow$$
 2Ti₃C₂ + Li₃AlF₆
+ AlCl₃ + 3LiCl + 3H₂. (2)

The stirring reaction at room temperature was continued for 12, 24, and 48 h to obtain different batches of samples, marked as M12h, M24h, and M48h, respectively. After the stirring reaction was complete, this slurry solution was poured slowly into 40 ml of deionised water dropwise. During the etching reaction, the reaction medium becomes highly acidic. Therefore, it needs to be neutralised. The solution was washed with DI water using centrifugation at a rotation speed of 13 000 rpm until the pH reached 7. After centrifugation at a rotation speed of 12 000 rpm, it was observed that the solution had not settled completely, even after centrifugation. This is because the layers of the etched $Ti_3C_2T_x$ MXene were peeled off, and the supernatant is retained. At this stage, the mixture was centrifuged at a rotation speed of 3500 rpm and separated the supernatant solution from the sedimented sample. The supernatant was then centrifuged at a rotation speed of 16 000 rpm, and the $Ti_3C_2T_x$ MXene was collected under wet conditions. The final Ti₃C₂T_r MXene sample was dried in a vacuum oven at 60 °C for 8 h. Finally, the Ti₃C₂T_x MXene sample was collected in powder form for further characterisation, reaction, and property measurements.

2.3. Synthesis of the β -Ni(OH)₂/Ti₃C₂T_x composite

For the preparation of the β -Ni(OH)₂/Ti₃C₂T_x composite samples, a hydrothermal technique was followed [22]. 50 mg of as-prepared Ti₃C₂T_x powder was dispersed in 50 ml of DMF by ultrasonic vibration for 10 min. An aqueous solution of 0.1 M Ni(OCOCH₃)₂,4H₂O mixed with 0.2 M NH₄OH solution was prepared. 10 ml of this solution was added to the previous dispersion of $Ti_3C_2T_x$ powder in DMF. The entire solution was transferred into an iron-lined autoclave, and a hydrothermal reaction was performed for 12 h at 180 °C. After the completion of the hydrothermal reaction, the final solution was washed by centrifugation. The $Ti_3C_2T_x$ nanosheets, decorated with β -Ni(OH)₂ flakes, are heavy and sedimented at a lower centrifugation speed (8000 rpm). The Ti₃C₂T_x nanosheets, which remained in the supernatant even after centrifugation, were removed because of their lack of attachment to the β -Ni(OH)₂ nanosheets on their surface and interlayer spacing. A large increase in the interlayer spacing of the (002) planes was observed, as discussed in the experimental section, after the hydrothermal reaction, indicating the growth of β -Ni(OH)₂ nanosheets within the interlayer spacing. The final composite sample, in powder form, was collected after drying in a vacuum oven at 60 °C for 8 h.

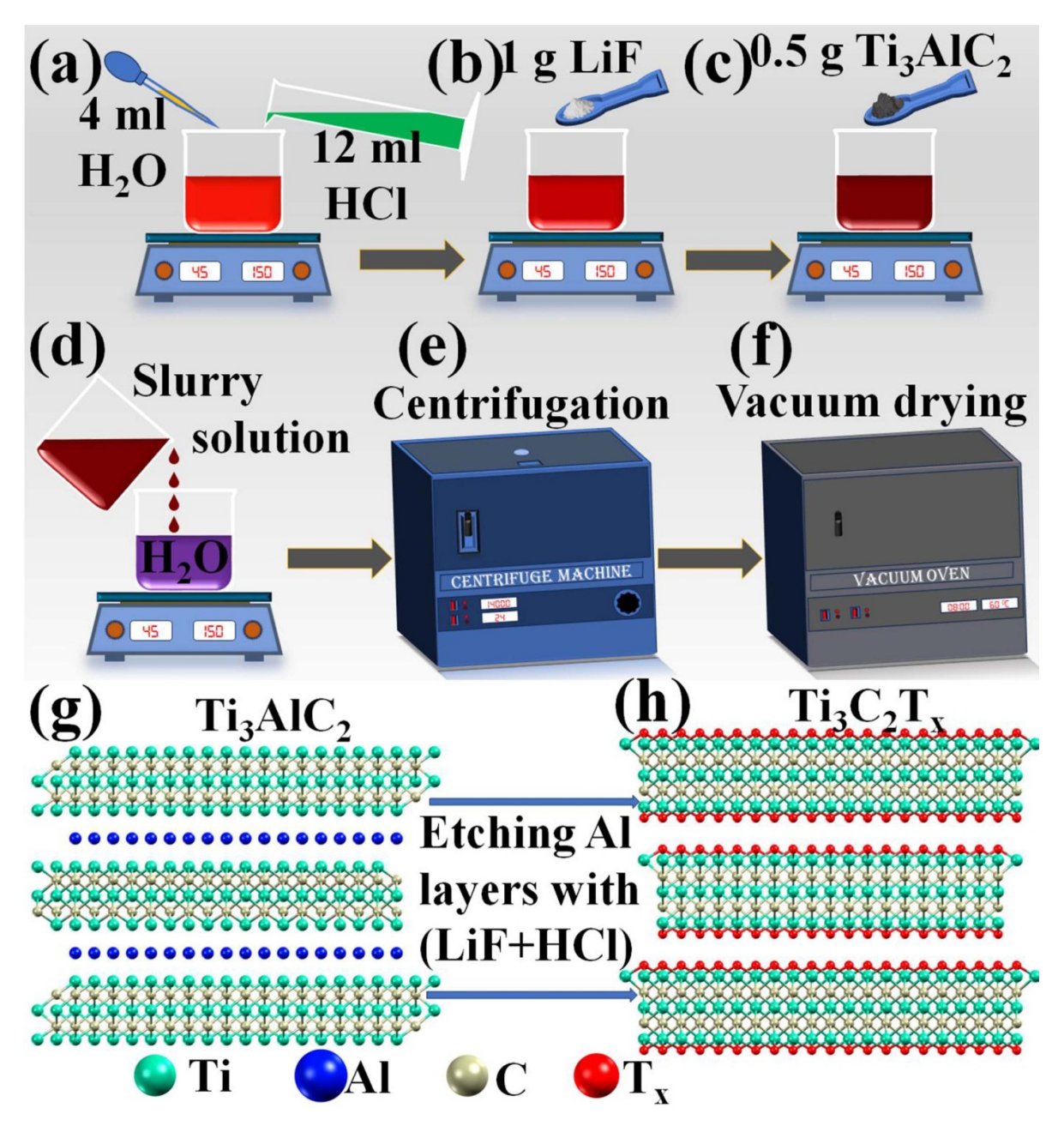


Figure 1. (a)–(f) Scheme of the synthesis of $Ti_3C_2T_x$ MXene. (g) Staking of Ti_3AlC_2 (MAX) layers with Al. (h) Stacking of $Ti_3C_2T_x$ MXene layers after etching of Al atoms from MAX.

2.4. Characterisation techniques

Atomic force microscopy (AFM) was performed on an MFP-3D Origin AFM machine (Asylum Research, Oxford Instruments, USA) to characterise the as-prepared samples. X-ray diffraction (XRD) was performed with a D8 Advance Diffractometer (Bruker, USA). An x-ray beam of the Cu $K\alpha$ line ($\lambda=1.54$ Å) was used for the XRD measurements. The structural and microstructural details are obtained from the Rietveld refinement of the XRD data [23]. To perform the Rietveld refinement, MAUD 2.99 software was used [24]. To determine the binding energy positions for the dif-

ferent elements, present within the samples, x-ray photoelectron spectroscopy (XPS) was performed on a PHI-5000 VersaProbe-III XPS machine (Physical Electronics, USA). To understand the sample morphology and elemental analysis, high-resolution transmission electron microscopy (HRTEM) and electron-dispersive x-ray spectroscopy (EDX) was performed on a JEM-2100 Plus electron microscope (JEOL, Japan). Raman spectroscopy was performed on a T64000 Raman spectroscope (HORIBA Scientific, Japan) to determine the different vibrational bonds present within the samples. A monochromatic LASER source with a wavelength of 532 nm was used to perform the Raman spectroscopy.

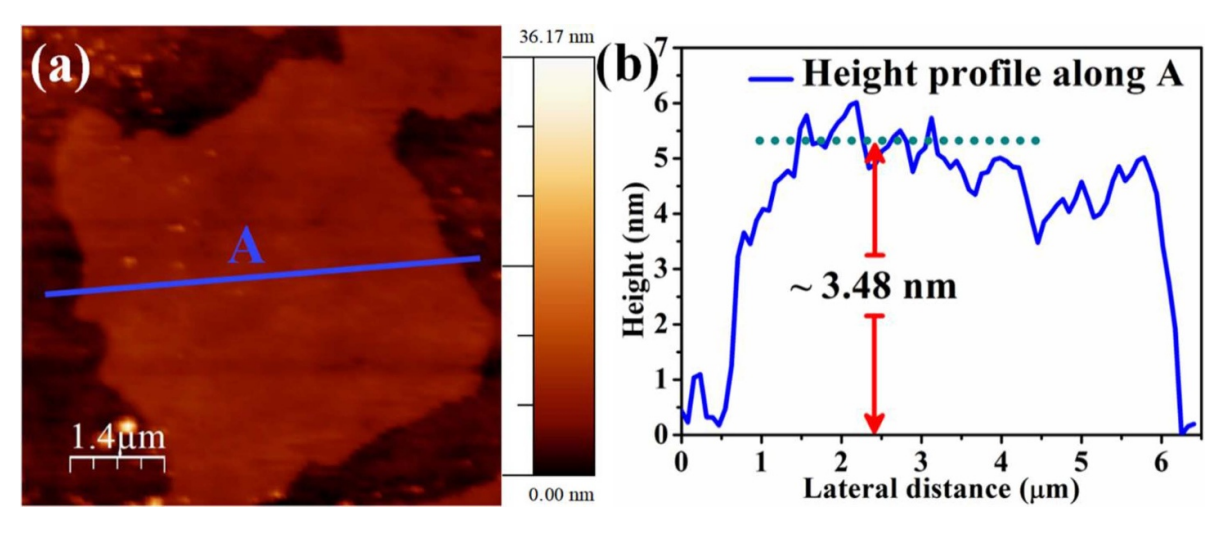


Figure 2. (a) AFM image of 2D Ti₃C₂T_x MXene micro-sheets. (b) The corresponding height-profile of the 2D Ti₃C₂T_x along the line A.

3. Results and discussion

3.1. Visualisation of ultrathin Ti₃C₂T_x MXene microsheets using atomic force microscopy

In the study of the magnetic properties of 2D $Ti_3C_2T_x$ MXene sheets and their interfacial interactions with decorated β -Ni(OH)₂ nanosheets, the essential requirement is to obtain ultrathin Ti₃C₂T_x MXene sheets with sufficiently large lateral dimensions. The theoretical thickness of the monolayer Ti₃C₂ MXene sheet is approximately 1 nm, whereas an experimental study suggested that this thickness is approximately 1.5 nm [25, 26]. As discussed in the synthesis section, etching Al atoms from the Ti₃AlC₂ MAX phase, followed by proper centrifugation, produces ultrathin 2D Ti₃C₂T_x sheets. The AFM image and height profile, as shown in figure 2, reveal that the thickness of the sheet is approximately 3.48 nm, corresponding to three layers of Ti₃C₂T_r MXene. The average lateral dimension of approximately 5.5 μ m indicates the sufficiently large lateral extent of the 2D $Ti_3C_2T_x$ MXene sheets. A surface roughness of approximately 1 nm indicates the surface cleanliness of the as-grown sheets. These clean ultrathin (~three-layered) 2D Ti₃C₂T_x MXene micro sheets were used for further reaction, characterisation and property measurements.

3.2. Rietveld refinement of x-ray diffraction

To understand the crystal structure and synthesis mechanism of the $Ti_3C_2T_x$ MXene by etching Al layers from the parent MAX (Ti_3AlC_2) phase, the x-ray diffraction (XRD) measurements were performed of the samples at different stages of synthesis. The analysis was started with Rietveld refinement of the XRD profile, as shown in figure 3(a), of the commercially purchased parent Ti_3AlC_2 (MAX) phase. Ti_3AlC_2 has a layered hexagonal structure with two formula units in a unit cell with a space group $P6_3/mmc$. In the XRD profile of the Ti_3AlC_2 crystal, the (014) peak indicates lattice symmetry

due to the Al layers, whereas the in-plane (002) peak indicates the crystal symmetry of the in-plane layers. The 2θ value of 9.7° for the (002) plane indicates an in-plane lattice spacing of 9.0 Å. The absence of additional peaks and the wellfitted profile indicate the phase purity of the starting precursor material. After etching the Ti₃AlC₂ crystal for 12 h, it was found that the peaks for the $Ti_3C_2T_x$ phase along with the Ti₃AlC₂ phase in the XRD profile, as shown in figure 3(b), of sample M12h. It was found that the in-plane peak, i.e. the peak for the (002) plane, appears at lower 2θ values. In the XRD profile, as shown in figure 3(c), for the M24h sample, it was found that the peaks corresponding to the Ti₃C₂T_r phase and the Ti₃AlC₂ phase. However, here, the peak intensity and the number of peaks corresponding to the Ti₃AlC₂ phase decreased. For the final MXene sample, i.e. for M48h, there is no peak corresponding to the Ti₃AlC₂ phase in the XRD profile, as shown in figure 3(d). Interestingly, the (002) planes at two different 2θ positions appeared for all three $Ti_3C_2T_x$ samples (M12h, M24h, and M48h). For the M12h sample, the (002) peak appears at 6.75° and 7.65°, corresponding to lattice spacings of 13.07 and 11.50 Å, respectively, whereas for the M24h sample, the (002) peak appears at 6.75° and 7.64°, corresponding to lattice spacings of 13.07 and 11.54 Å, respectively. For the M48h sample, the (002) peak appears at 6.71° and 7.38°, corresponding to lattice spacings of 13.15 and 11.95 Å, respectively. There are two reasons for the increase in the lattice spacing and, hence, the shift of the (002) peaks to lower 2θ values. During the etching of Al from the Ti₃AlC₂ phase, there is a generation of hydrogen gas, which creates pressure to increase the interlayer spacing [1, 27]. The production of hydrogen gas was observed through vigorous bubbling at the beginning of the reaction. The violent bubbling within the interlayer spacing of the Ti₃C₂ layers creates a pressure to enhance the interlayer spacing between two adjacent layers. Additionally, each layer is functionalised with different functional groups (T_x) , such as -F, -O, -OH, and -Cl. As a result, the interlayer spacing increases, and the (002) plane shifts to a lower 2θ value.

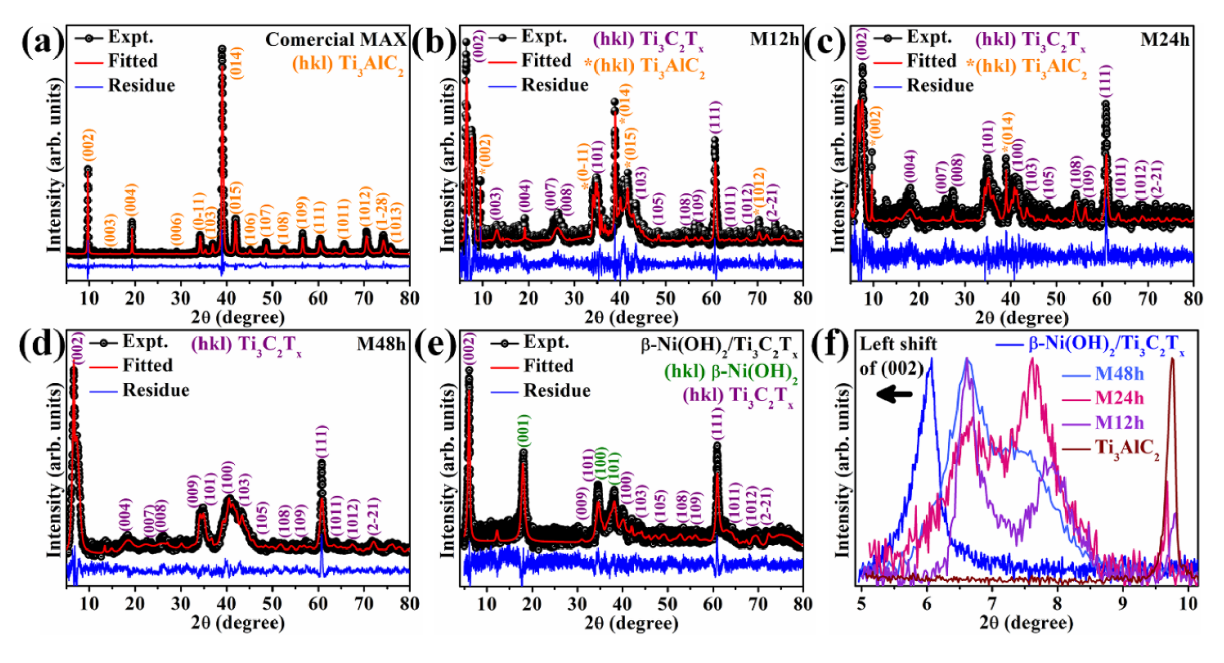


Figure 3. XRD profile of (a) commercial Ti₃AlC₂ MAX phase, (b) M12h sample, (c) M24h sample, (d) M48h sample, and (e) β-Ni(OH)₂/Ti₃C₂T_x composite sample. (f) Comparative position and shifting of (002) plane from Ti₃AlC₂ MAX to different Ti₃C₂T_x MXene sheets.

Even in the absence of the connecting element (Al), these layers are stacked with greater interlayer spacing, as indicated by the (002) peak at a lower 2θ value. The generation of hydrogen gas and the number of functional groups depend entirely on the synthesis conditions, such as the nature and number of etchants. Thus, the increase in the lattice spacing due to these two effects depends on the synthesis environment. During rigorous centrifugation, some layers peel off from the stack, and the interlayer spacing increases. This additional increase in the lattice spacing further shifts the (002) peak positions for a few crystal layers. Thus, two peak positions for the (002) plane were observed in the three $Ti_3C_2T_x$ samples (M12h, M24h, and M48h). Eventually, with the etching of the Al layers, pressure is produced by the generated hydrogen gas, and centrifugation contributes to the lattice increase; hence, the (002) peak shifts to a lower 2θ value. In the case of the composite sample, there was growth of β -Ni(OH)₂ nanoflakes on both surfaces of each $Ti_3C_2T_x$ layer. Due to the uniform growth of β -Ni(OH)₂ nanoflakes within the interlayer spacing of Ti₃C₂T_x nanosheets produce additional interlayer spacing. The β -Ni(OH)₂-decorated Ti₃C₂T_x nanosheets were separated by controlling the centrifugation speed from the undecorated $Ti_3C_2T_x$ nanosheets. The stacking of $Ti_3C_2T_x$ nanosheets was fully decorated with β -Ni(OH)₂ nanosheets sedimented at a lower centrifugation speed of 8000 rpm. The supernatant solution containing undecorated Ti₃C₂T_x nanosheets was washed away. Due to the presence of β -Ni(OH)₂ nanosheets within the interlayer space of the $Ti_3C_2T_x$ nanosheets, the (002) peaks were found, as shown in figure 3(e), at a lower 2θ of 6.1° corresponding to a lattice spacing of 14.4 Å. To better visualise the gradual shift of the (002) plane from the MAX phase to the composite sample, the (002) peak regions were plotted for all the samples in a single panel, as shown in figure 3(f). All the

parameters obtained from the Rietveld refinement of the XRD profiles are summarised in table 1. The lattice parameters, i.e. a and c, of $Ti_3C_2T_x$, as presented in table 1, differ from the lattice parameters of pure Ti_3C_2 , with values a = b = 3.06 Åand c = 15.11 Å. Because of the different functional groups, the lattice parameters decrease for a and b, whereas the lattice parameter along the c axis increases [28]. For the composite sample, the (002) peak was found at a lower 2θ value and an increase in the interlayer spacing to 14.4 Å. The increase in the lattice parameter along the c-axis increases to a large value of 26.41 Å. To further confirm the presence of the as-grown β -Ni(OH)₂ phase in the synthesis technique discussed in this article, the XRD measurements of the bare β -Ni(OH)₂ crystal was also performed. The supplementary materials include the detailed XRD analysis of the bare β -Ni(OH)₂ crystal. All the bare β -Ni(OH)₂ peaks, as presented in figure S1, are well fitted with the standard reference positions and confirm the phase purity. Hence, the value of the lattice parameter is consistent with the experimental observations. For refinement, the crystallographic information files (CIFs) with the following card nos. mp-3747 (Ti₃AlC₂, hexagonal phase), mp-1094034 (Ti₃C₂, hexagonal phase) and mp-27912 (Ni(HO)₂, trigonal phase) from the Materials Project website were used [29].

3.3. X-ray photoelectron spectroscopy

Figures 4, 5 and 6 show the XPS spectra of the bare- $Ti_3C_2T_x$ MXene, bare- β -Ni(OH)₂ and β -Ni(OH)₂-decorated $Ti_3C_2T_x$ MXene samples, respectively. In the case of the bare- $Ti_3C_2T_x$ MXene, as shown in figure 4(a), the signature peaks corresponding to compositional elements (Ti, C) in the $Ti_3C_2T_x$ along with different functional groups (such as -F, -O and -OH) were found. The absence of any

Table 1. Parameters obtained from Rietveld refinement of the XRD data.

Sample	Crystal phases	Volume fraction (%)	Lattice parameters (Å)	Average crystallite size (Å)	RMS lattice strain	Goodness of Fit
Commercial MAX	Ti ₃ AlC ₂	100	$a = 3.06 \pm 0.01$ $b = 3.07 \pm 0.01$ $c = 18.55 \pm 0.03$ $\alpha = 89.89 \pm 0.01$ $\beta = 89.99 \pm 0.02$ $\gamma = 119.62 \pm 0.02$	870 ± 1	8.3×10^{-5}	1.07
	$Ti_3C_2T_x$	71	$a = 3.05 \pm 0.01$ $c = 23.01 \pm 0.03$	169 ± 9	2.7×10^{-2}	
M12h	Ti ₃ AlC ₂	29	$a = 3.10 \pm 0.01$ $b = 3.04 \pm 0.01$ $c = 18.53 \pm 0.03$ $\alpha = 92.09 \pm 0.01$ $\beta = 89.03 \pm 0.02$ $\gamma = 120.52 \pm 0.05$	$221 \pm 1 \qquad \qquad 3.0 \times 10^{-3}$		2.95
	$Ti_3C_2T_x$	83	$a = 3.05 \pm 0.02$ $c = 23.07 \pm 0.08$	363 ± 7	1.1×10^{-3}	
M24h	Ti ₃ AlC ₂	17	$a = 3.09 \pm 0.01$ $b = 3.19 \pm 0.01$ $c = 18.02 \pm 0.05$ $\alpha = 99.32 \pm 0.03$ $\beta = 79.01 \pm 0.04$ $\gamma = 120.5 \pm 0.02$	113 ± 3	4.4×10^{-3}	2.63
M48h	$Ti_3C_2T_x$	100	$a = 3.03 \pm 0.01$ $c = 23.15 \pm 0.03$	740 ± 8	2.4×10^{-3}	1.97
	$Ti_3C_2T_x$	62	$a = 3.02 \pm 0.04$ $c = 26.41 \pm 0.06$	362 ± 8	7.8×10^{-3}	
β-Ni(OH) ₂ decorated MXene	β-Ni(OH) ₂	38	$a = 2.99 \pm 0.01$ $b = 3.06 \pm 0.05$ $c = 4.96 \pm 0.04$ $\alpha = 96.61 \pm 0.01$ $\beta = 83.56 \pm 0.01$ $\gamma = 119.89 \pm 0.01$	159 ± 1	5.0×10^{-3}	1.52

peaks for Al indicates the complete removal of the Al layers from the Ti_3AlC_2 MAX phase to the $Ti_3C_2T_x$ MXene phase. Similarly, in the survey scan spectra of bare β -Ni(OH)₂, as shown in figure 5(a), signature peaks for the compositional elements, viz., Ni and O were found. Similarly, in the case of β - $Ni(OH)_2$ -decorated $Ti_3C_2T_x$ MXene, as shown in figure 6(a), the signature peaks for different compositional elements of both $Ti_3C_2T_x$ and β -Ni(OH)₂ were found. To obtain the exact peak positions of the different compositional elements, a slow scan of the peak regions for Ti 2p, C 1s, O 1s, F 1s and Ni 2p for all three samples were performed and deconvoluted them with the proper profile fitting method. The exact peak positions for all the deconvoluted spectra are tabulated in table 2. The Ti 2p spectra for both the bare- $Ti_3C_2T_r$ MXene (figure 4(b)) and β -Ni(OH)₂-decorated Ti₃C₂T_x MXene (figure 6(b)) samples show $2p_{3/2}$ and $2p_{1/2}$ spin-orbital splits of the three peaks. As the energy positions of the Ti 2p spectra for the C-Ti bond are influenced by local bonding with the terminated functional groups (T_x) , three kinds of influences and three sets of peaks

corresponding to the Ti 2p bonds, viz., C-Ti-T_O, C-Ti-T_{F,O} and C-Ti-T_O were observed [30, 31]. The peaks near 454.7 $(2p_{3/2})$ and 460.8 $(2p_{1/2})$ eV correspond to the C-Ti-T_O bond. The peaks near 456.1 $(2p_{3/2})$ and 464.6 $(2p_{1/2})$ eV correspond to the C-Ti- $T_{F,O}$ bond. The peaks near 459.0 (2p_{3/2}) and $466.3 (2p_{1/2})$ eV correspond to the C–Ti– T_F bond. Figures 4(c)and 6(c) show high-resolution XPS spectra of the C 1s peak of the bare-Ti₃C₂T_x MXene and β -Ni(OH)₂-decorated Ti₃C₂T_x MXene samples, respectively. Two major peaks near 281.41 and 284.87 eV were found in both spectra, corresponding to Ti-C-Ti and C-C bonds, respectively [30, 31]. The Ti-C-Ti peak represents the characteristic peak of the $Ti_3C_2T_x$ MXene network, whereas the C-C bond represents the graphitic carbon networks at the C-terminated edges. The hump(s) in the spectra for both the samples (figures 4(c) and 6(c)) at the knee near the binding energy of 286.78 and 288.36 eV correspond to the C–O, C=O, etc, bonds coming from C-based impurities such as COH, COO, CH_r, etc [31]. Three component peaks in the O 1s spectra, as shown in figures 4(d), 5(b), and 6(d),

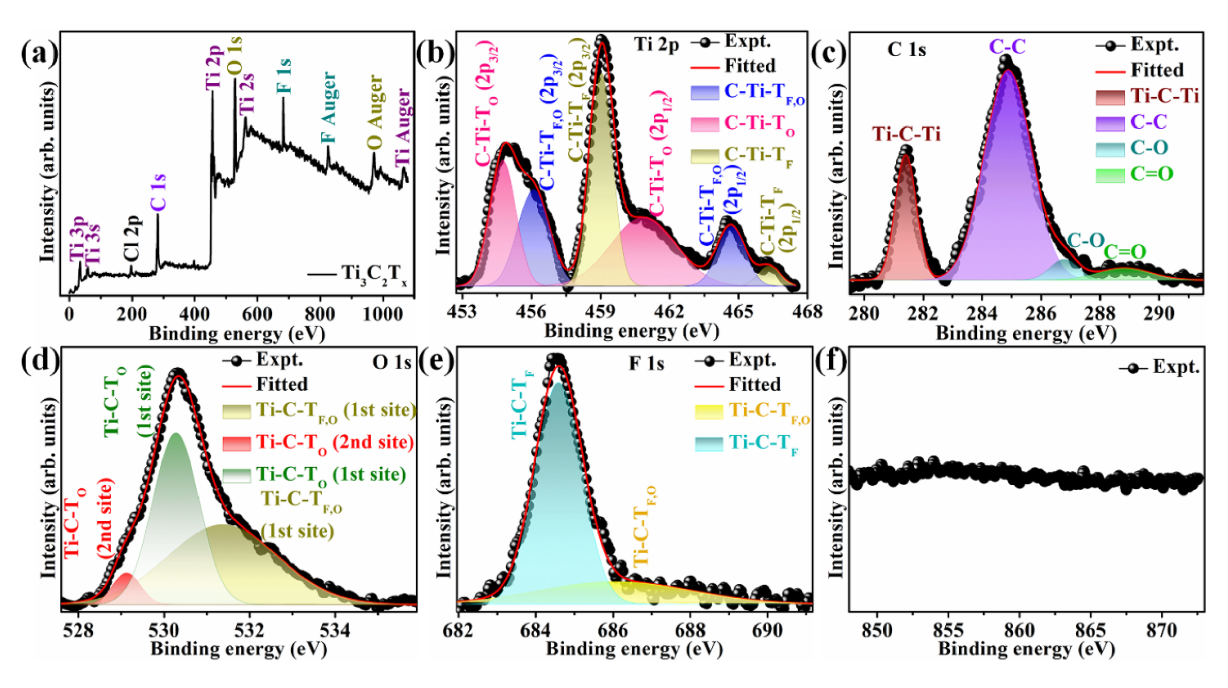


Figure 4. (a) XPS spectra of bare 2D Ti₃C₂T_x MXene sample. High-resolution scan in the region of (b) Ti 2p, (c) C 1s, (d) O 1s, (e) F 1s, and (f) Ni 2p region.

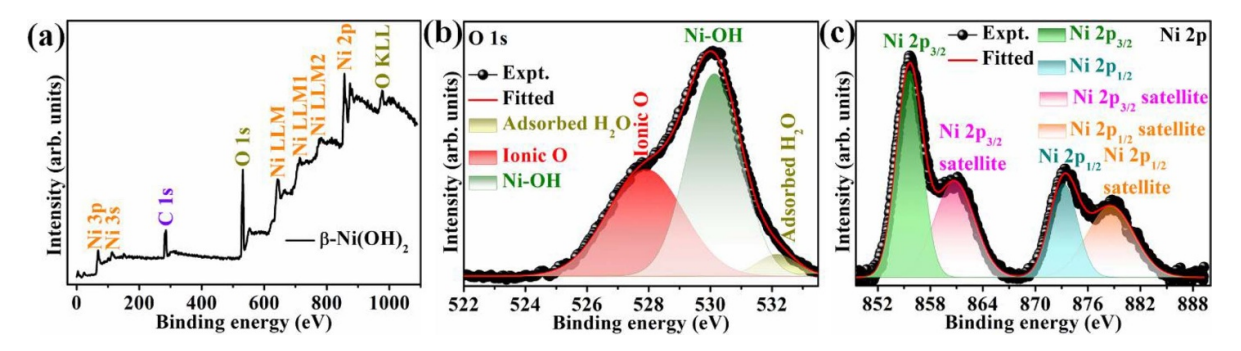


Figure 5. (a) XPS spectra of bare β -Ni(OH)₂ sample. High-resolution scan in the region of (b) O 1s, and (c) Ni 2p region.

for all three samples (bare-Ti₃C₂T_x MXene, bare β -Ni(OH)₂ and β -Ni(OH)₂-decorated Ti₃C₂T_r MXene, respectively) were found. The three peaks near 529.1, 530.2 and 531.3 eV in the O 1s spectra for the bare- $Ti_3C_2T_x$ sample correspond to $Ti-C-T_O$ (2nd site), $Ti-C-T_O$ (1st site), and $Ti-C-T_{EO}$ (1st site), respectively [31]. The three component peaks near 527.9, 530.1 and 532.1 eV in the O 1s spectra for the bare β -Ni(OH)₂ correspond to ionic oxygen; the Ni-OH bond and the bond come from adsorbed H₂O, respectively. In the case of the composite sample, three peaks approximately at the same positions were also observed, but there was a difference in the nature of the peaks. The three peaks near 529.0, 529.9, and 531.3 eV correspond to ionic oxygen; the Ni-OH bond and the bond come from adsorbed H₂O [31, 32]. These three peaks may overlap with the three characteristic peaks of O 1s (viz., Ti-C-T_O (2nd site), Ti-C-T_O (1st site), and Ti-C-T_{EO} (1st site) bonds) due to the adsorbed functional groups (T_x) of $Ti_3C_2T_x$. The influence of different terminal functional groups (T_x such as F and O) was also confirmed by observing their presence in the XPS spectra for both the bare- $Ti_3C_2T_x$ MXene and β - $Ni(OH)_2$ -decorated $Ti_3C_2T_x$ MXene samples. Two peaks in the F 1s spectra (figures 4(e) and 6(e)) for both samples were found. In the bare- $T_{i_3}C_2T_r$ sample, as shown in figure 4(e), the intense peak near 684.5 eV corresponds to the C-Ti-T_F bond, whereas the hump near 686.0 eV corresponds to the C-Ti-T_{F,O} bond [31]. For the bare- $Ti_3C_2T_x$ MXene sample, the F 1s peak is quite close to the reported value, whereas for the composite sample, the F 1s peak (figure 6(e)) occurs at a slightly greater value (684.9 and 687.3 eV), as presented in table 2. The reason is the charge transfer from the anionic p-site of T_F to the d-site of the transition metal, as discussed later. Compared with the bare $Ti_3C_2T_x$, as presented in table 3, the average peak shifting of the F 1s spectra of the composite sample is 0.8 eV. Usually, most of the T_F groups are washed away during heat treatment. However, due to the bond formation with the Ni atoms of β -Ni(OH)₂, some T_F groups cannot be removed; hence, the presence of these groups in the XPS spectra of the composite sample was observed even after hydrothermal treatment. The Ni 2p spectra of the bare β -Ni(OH)₂ and the composite sample are shown in figures 5(c) and 6(f). In the Ni 2p spectrum of bare β -Ni(OH)₂, there are four component peaks near 855.5, 860.7, 873.2, and 878.5 eV. The peaks near 855.5 and

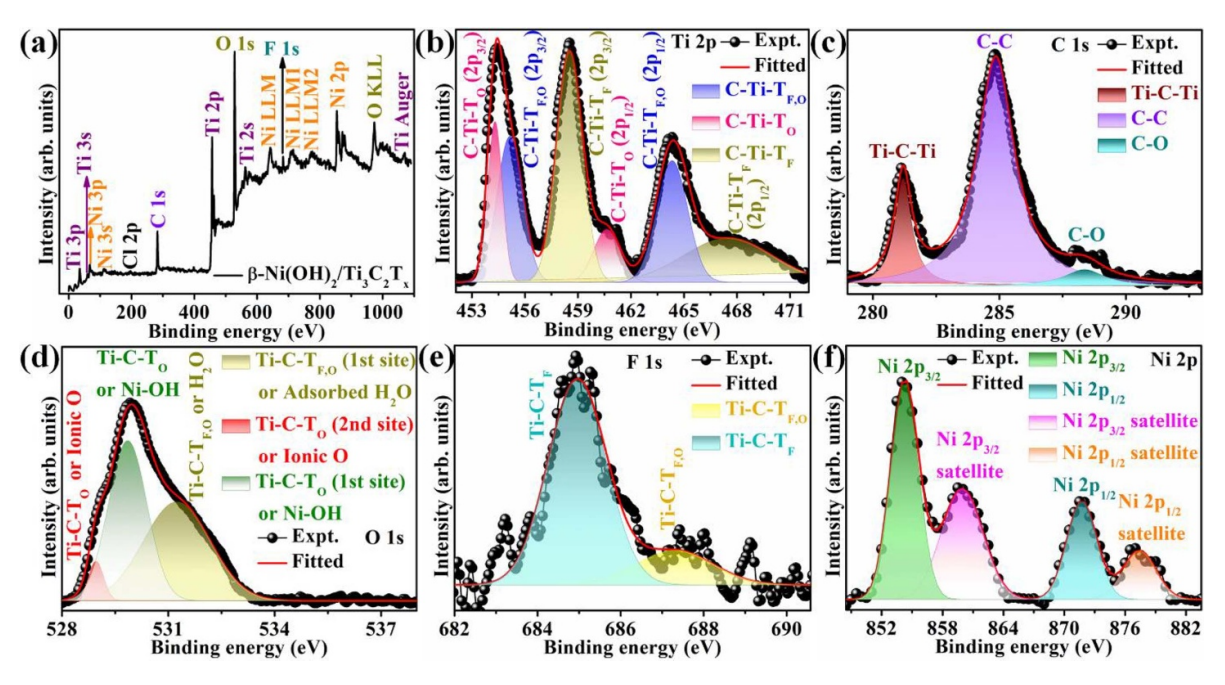


Figure 6. (a) XPS spectra of β -Ni(OH)₂/Ti₃C₂T_x composite sample. High-resolution scan in the region of (b) Ti 2p, (c) C 1s, (d) O 1s,1s, (e) F 1s, and (f) Ni 2p region.

873.2 eV correspond to the Ni $2p_{3/2}$ and $2p_{1/2}$ states, whereas the peaks near 860.7 and 878.5 eV correspond to shake-up satellites [32]. Whereas, the Ni 2p spectrum of the composite sample consists of four component peaks near 854.2, 859.9, 871.7, and 877.4 eV. The peaks near 854.2 and 871.7 eV correspond to the Ni 2p_{3/2} and 2p_{1/2} states, whereas the peaks near 859.9 and 877.4 eV correspond to shake-up satellites [32]. Compared with the bare β -Ni(OH)₂, as presented in table 3, it was observed that all the component peaks of Ni 2p of the composite sample had lower binding energies [32]. The average peak shift for the Ni 2p_{3/2} bands is approximately 1.3 eV, whereas that for the Ni $2p_{1/2}$ bands is approximately 1.8 eV (table 3). The reason behind the shift in the Ni 2p spectra to a lower binding energy is the charge sharing from the negatively charged environment of different functional groups (T_r) , especially T_F. Like in other composites of MXene, as suggested by Xie et al, interfacial charge transfer occurs from negatively charged T_x (e.g. –F) to positively charged cation (Ni²⁺) when β -Ni(OH)₂ grows on Ti₃C₂T_x and forms ionic-like bonds [33]. Because of this bond formation, even after treating the $Ti_3C_2T_x$ via a hydrothermal treatment, the F atoms did not wash away completely in the composite sample. Previously reported photoconductive and x-ray photoelectron spectroscopy data established the phenomenon of charge transfer from the anionic p-orbital (F 2p) to the transition metal d-orbital (Ni 3d) [34, 35]. The well-known core hole effect in XPS spectra influences the F 1s and Ni 2p spectra [36]. The partial transfer of electrons from the F p-orbitals of $Ti_3C_2T_x$ to the Ni d-orbitals of β -Ni(OH)₂ reduces the binding energy of core-level electrons in Ni. Hence, the shifting of Ni 2p states to lower binding energy regions was observed, and the modification of 2p shake-up satellites (table 3) was found. Similarly, the charge transfer from the p-orbital of F influences the F 1s spectrum in XPS; hence, this transfer occurs at a higher binding energy (table 3). The absence of any peak in the binding energy region of 845–875 eV, as shown in figure 4(f), for the bare- $Ti_3C_2T_x$ MXene sample confirms that the peaks in the same region of the composite sample are not from any functional groups/precursor impurities of MXene but from the Ni 2p states. This charge sharing to the Ni atoms of β -Ni(OH)₂ results in the induced ferrimagnetism discussed later in section 3.7 to the β -Ni(OH)₂-decorated $Ti_3C_2T_x$ MXene sheets. The mechanism of the induction of the magnetic moment due to charge transfer is discussed in detail in a later section (section 3.7).

3.4. Transmission electron microscopy

The transmission electron microscopy (TEM) analysis was performed to determine the morphology of the as-prepared samples. Figure 7(a) shows the overall image of the β - $Ni(OH)_2$ -decorated $Ti_3C_2T_x$ sheet. To confirm the lattice parameters and hence the crystal phases, selected area electron diffraction (SAED) of the sample was performed. In the SAED pattern, as shown in figure 7(b), the diffraction spots for both the β -Ni(OH)₂ and Ti₃C₂T_x crystals were observed. A pair of spots for the parallel sets of planes (004) and (111) of the Ti₃C₂T_x crystal with lattice spacings of 0.59 and 0.15 nm, respectively, were found. Spots for the (001), (011), and (110) parallel sets of planes of β -Ni(OH)₂ with lattice spacings of 0.46, 0.22, and 0.16 nm, respectively, were also found. For better visualisation and accurate measurement of the lattice spacing and phase confirmation, high-resolution transmission electron microscopy (HRTEM) was performed on the sample. The HRTEM image, as shown in figure 7(c), reveals an island of β -Ni(OH)₂ nanosheets growing on the surface of the $Ti_3C_2T_x$ crystal. For the sake of exact measurement of the lattice parameters of the signature planes of β -Ni(OH)₂, i.e. the (001) set of planes, an inverse fast Fourier transform

Table 2. Binding energy values of all the XPS spectra.

Samples	Elements	Components	Binding er	nergy (eV)
	Ti 2p	C–Ti–T _O C–Ti–T _{F,O} C-Ti-T _F	454.7 (2p _{3/2}) 456.1 (2p _{3/2}) 459.0 (2p _{3/2})	460.8 (2p _{1/2}) 464.6 (2p _{1/2}) 466.3 (2p _{1/2})
Bare-Ti ₃ C ₂ T _{x} MXene	C 1s	Ti-C-T _x C-C C-O C=O	281.4 284.8 286.7 288.8	
	F 1s	Ti-C-T _F Ti-C-T _{F,O}	684.5 686.0	
	O 1s	Ti–C–T _O (2nd site) Ti–C–T _O (1st site) Ti–C–T _{F,O} (1st site)	529.1 530.2 531.3	
	Ni 2p	Main peaks Shake-up satellites	855.5 (2p _{3/2}) 860.7 (2p _{3/2})	873.2 (2p _{1/2}) 878.5 (2p _{1/2})
β -Ni(OH) ₂	O 1s	Ionic O Ni–O Adsorbed H ₂ O	527.9 530.1 532.1	
	Ti 2p	C–Ti–T _O C–Ti–T _{F,O} C–Ti–T _F	454.3 (2p _{3/2}) 455.1 (2p _{3/2}) 458.5 (2p _{3/2})	460.6 (2p _{1/2}) 464.3 (2p _{1/2}) 467.4 (2p _{1/2})
2 NYOUN described To C. T.	C 1s	Ti-C-T _x C-C C-O	281.2 284.8 288.3	
β -Ni(OH) ₂ decorated Ti ₃ C ₂ T _x	F 1s	Ti-C-T _F Ti-C-T _{F,O}	684.9 687.3	
	O 1s	Ti-C-T _O (2nd site) or Ionic O Ti-C-T _O (1st site) or Ni-O Ti-C-T _{F,O} (1st site) or Adsorbed H ₂ O	529.0 529.9 531.3	
	Ni 2p	Main peaks Shake-up satellites	854.2 (2p _{3/2}) 859.9 (2p _{3/2})	871.7 (2p _{1/2}) 877.4 (2p _{1/2})

Table 3. Major shift in binding energy in composite sample in comparison with their bare form.

Binding energy (eV)						
Element	Orbitals	Composite sample	Bare sample	Shifting of binding energy (eV)		
Ni 2p	2p _{3/2}	854.2	855.5	-1.3		
	2p _{3/2} satellite	859.9	860.7	-0.8		
	$2p_{1/2}$	871.7	873.2	-1.5		
	2p _{1/2} satellite	877.4	878.5	-1.1		
F 1s	Ti-C-T _F	684.9	684.5	+0.4		
	$Ti-C-T_{F,O}$	687.3	686.0	+1.3		

(IFFT) was performed, as shown in figure 7(d). The lattice spacing is measured as 0.46 nm, which matches the lattice spacing of the (001) plane of β -Ni(OH)₂. Thus, it can be concluded that β -Ni(OH)₂ nanosheets grow on the Ti₃C₂T_x planes. Electron diffraction x-ray spectroscopy (EDXS), as shown in figure 7(e), was also performed to obtain a rough estimation of the sample's elemental composition. All the compositional elements (Ti, C and F from Ti₃C₂T_x and Ni and O from β -Ni(OH)₂) were in the EDXS spectrum. To visualise the uniformity of the elements' distribution within the

samples, we have performed the elemental mapping, as shown in figure S2 of supplementary material. It also establishes the presence of all the compositional elements of the composites. The absence of other elements in the EDXS spectra indicates the phase purity of the sample.

3.5. Raman spectroscopy

The Raman spectroscopy was performed on the as-synthesised $Ti_3C_2T_x$ MXene and β -Ni(OH)₂-decorated MXene samples.

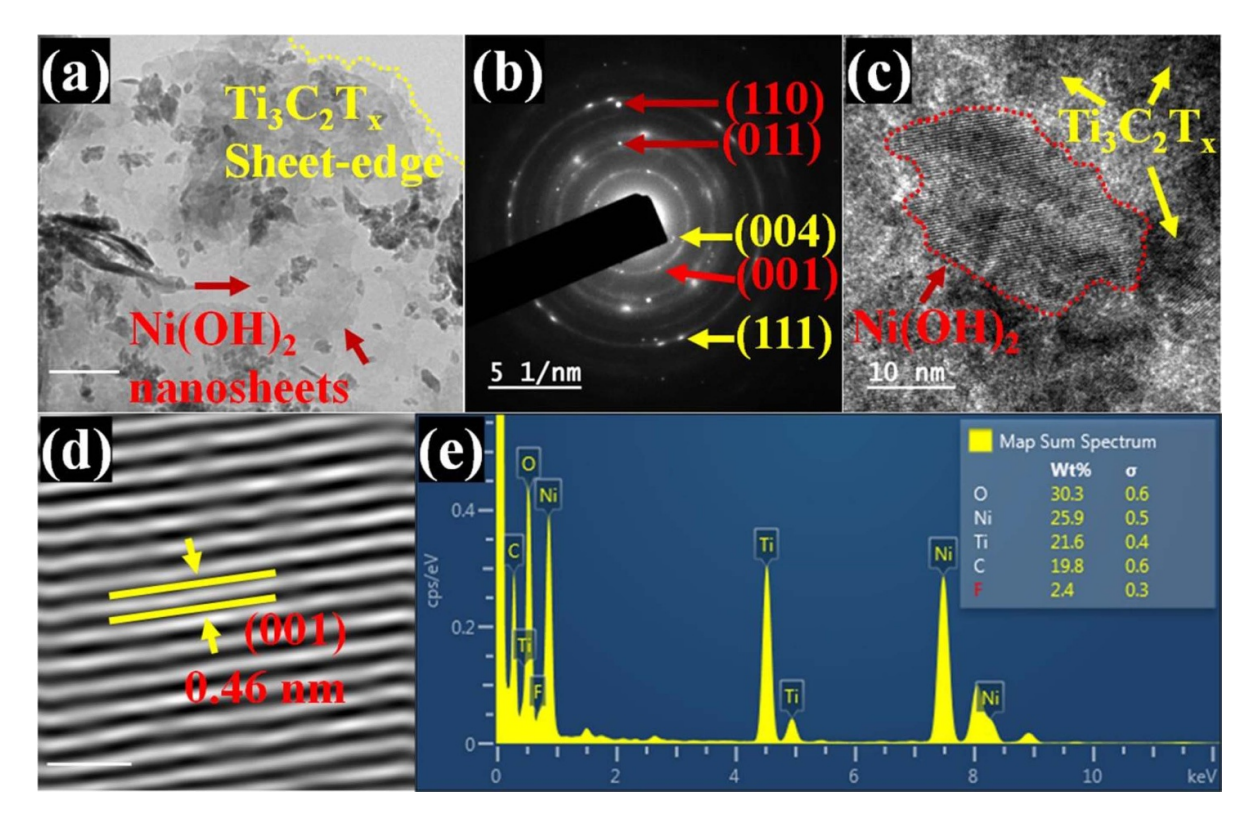


Figure 7. (a) TEM image of β -Ni(OH)₂ nanosheet decorated 2D Ti₃C₂T_x MXene sheet. (b) SAED pattern of the β -Ni(OH)₂/Ti₃C₂T_x composite sample. (c) High-resolution TEM image of β -Ni(OH)₂ nanosheet grown on Ti₃C₂T_x MXene sheet. (d) Corresponding IFFT pattern for better visualization of lattice spacing. (e) EDXS spectra of β -Ni(OH)₂/Ti₃C₂T_x composite sample.

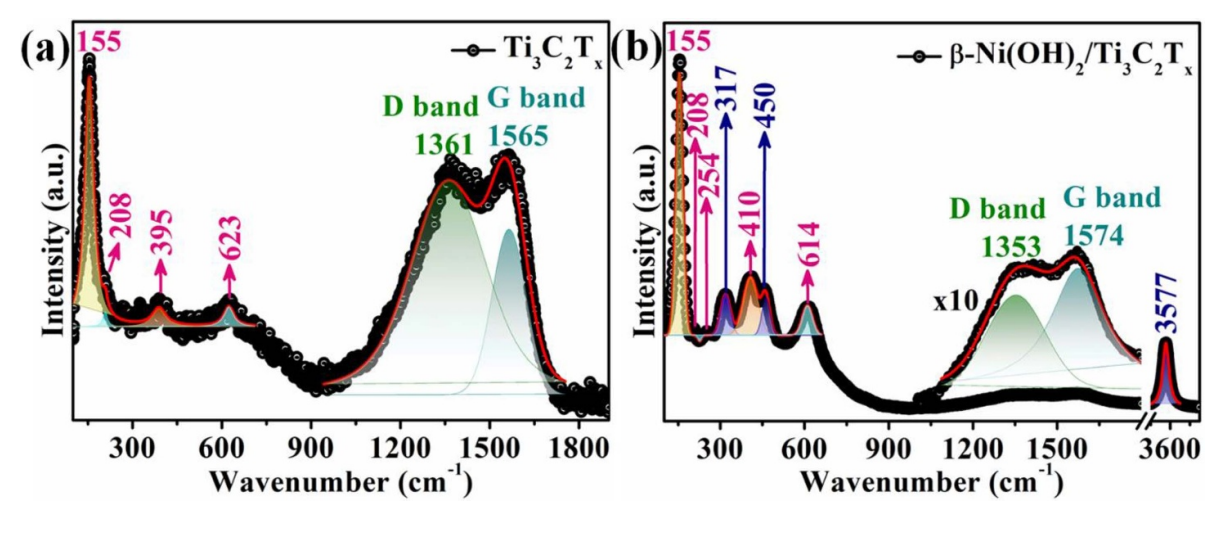


Figure 8. Raman spectra of (a) bare 2D $Ti_3C_2T_x$ nanosheet sample, and (b) β -Ni(OH)₂/ $Ti_3C_2T_x$ composite sample.

As shown in figure 8(a), the Raman spectrum of the bare- $Ti_3C_2T_x$ MXene sample shows characteristic peaks at 155, 395, 629, 1361, and 1565 cm⁻¹ [37, 38]. The peaks at 395 and 629 cm⁻¹ correspond to the vibration of the C–Ti–O bond, whereas the peak at 155 cm⁻¹ is due to the stretching vibration of the Ti–O bond [38]. The broad peaks near 1361 and 1565 cm⁻¹ correspond to the D and G bands of the defective carbon species present within the $Ti_3C_2T_x$ MXene [37]. As shown in figure 8(b), the Raman spectrum of the β-Ni(OH)₂/ $Ti_3C_2T_x$ composite sample shows the characteristic

peaks of both $Ti_3C_2T_x$ and β -Ni(OH)₂. The peaks near 155, 208, 254, 317, 410, 450, 614, 1353, 1574, and 3577 cm⁻¹ were found for the composite sample. The peaks near 410 and 614 cm⁻¹ correspond to the vibrational mode of the C–Ti–O bond, whereas the peak near 254 cm⁻¹ corresponds to the stretching vibrational mode of the Ti–O–Ti bond [38]. The peak near 155 cm⁻¹ is due to the stretching vibration of the Ti–O bond [38]. The broad peaks near 1353 and 1574 cm⁻¹ correspond to the D and G bands of the defective carbon species present within the $Ti_3C_2T_x$ MXene [37]. The peaks near

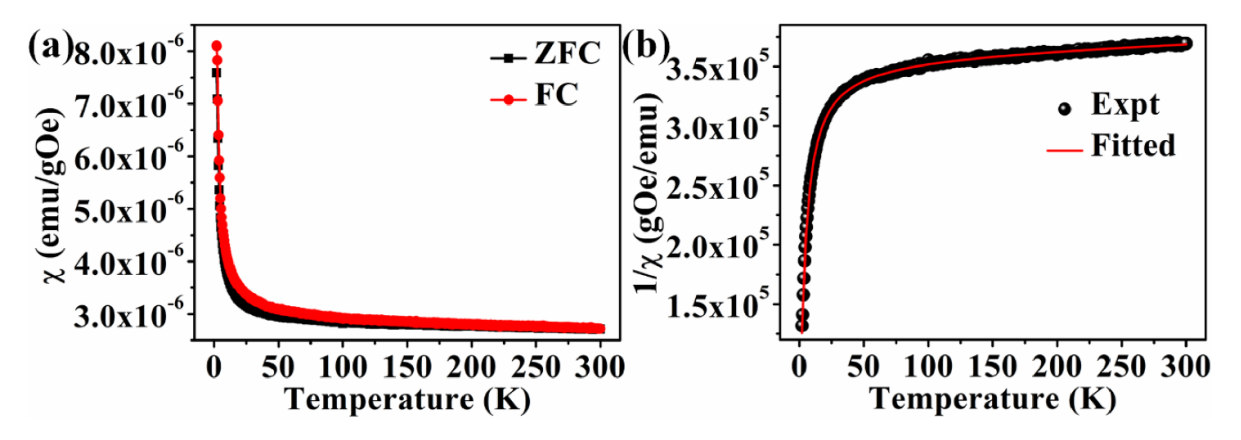


Figure 9. (a) The $\chi(T)$ data in both ZFC and FC mode of bare 2D $Ti_3C_2T_x$ nanosheet sample. (b) The corresponding inverse susceptibility data fitted with Neel equation.

317 and 450 cm⁻¹ correspond to the Ni–OH vibrational mode, and the peak in the higher frequency range near 3577 cm⁻¹ corresponds to the stretching vibration of the Ni–O bond of β -Ni(OH)₂ [39, 40]. Hence, the Raman spectra of both samples established the phases present within the bare-Ti₃C₂T_x MXene and β -Ni(OH)₂/Ti₃C₂T_x composite samples. The absence of any extra peaks within these ranges confirmed the absence of any artefacts or impurities.

3.6. Magnetic study of 2D Ti₃C₂T_x MXene sheets

To understand the magnetic behaviour of the bare-Ti₃C₂T_x MXene sheets, the susceptibility data as a function of temperature, i.e. $\chi(T)$ data, in both zero-field cooled (ZFC) and field-cooled (FC) modes were measured. The magnetisation data as a function of the magnetic field, i.e. the M(H) data were also measured. Figure 9(a) shows the $\chi(T)$ data in ZFC and FC modes for the bare 2D Ti₃C₂T_x MXene sheets. The $\chi(T)$ data show a paramagnetic-like behaviour throughout the whole temperature range, but the data are not fitted with the well-known Curie law $(\chi = \frac{C}{T})$. A bifurcation between the ZFC and FC data in the low-temperature region was also observed. To gain insight into the magnetic ordering within the bare-Ti₃C₂T_x MXene sheets, the inverse susceptibility $(\frac{1}{v} \text{ vs T})$ data was plotted. The inverse susceptibility data do not show linear paramagnetic behaviour. The typical behaviour of the inverse susceptibility data fits the Neel equation $(\frac{1}{\chi} = \frac{T}{C} + \frac{1}{\chi_0} - \frac{\sigma}{T - \theta})$ considered for antiferromagnetic or ferrimagnetic substances having two different sublattices [41]. The best fit (adj. $R^2 = 0.99$) of the data provides the different fitting parameters $C = 2.3 \times 10^{-3}$ emu K g⁻¹ Oe⁻¹, $\chi_0 = 2.77 \times 10^{-6}$ emu g⁻¹ Oe⁻¹, $\sigma = 1.29 \times 10^{6}$ K g Oe emu and $\theta = 3.5$ K. The configurations of the Ti atoms for the exposed surface and its interior plane are fairly different. The bonding of different functional groups, especially with T_F, provides the outer-plane Ti atoms with magnetic ordering opposite to that of the inner-plane Ti atoms. Hence, weak ferrimagnetic ordering is generated. A weak ferrimagnetic behaviour was also observed in the M(H) data. As shown in figure 10, the isothermal hysteresis curves at different temperatures for the bare-Ti₃C₂T_x MXene sample show weak

ferrimagnetic behaviour with negligible coercivity. Thus, it is concluded that the generated moment does not have any strong ordering between them.

3.7. Magnetic study of β -Ni(OH)₂-decorated MXene sheets

To understand the magnetic behaviour of the β -Ni(OH)₂decorated $Ti_3C_2T_x$ MXene sheets, the susceptibility as a function of temperature, i.e. $\chi(T)$ data, in both zero-field cooled (ZFC) and field-cooled (FC) modes was measured. The magnetisation data as a function of the magnetic field, i.e. the M(H) data was also measured. Figure 11(a) shows the $\chi(T)$ data in both the ZFC and FC modes for the β -Ni(OH)₂/Ti₃C₂T_x composite sample. Here, a ferrimagnetic-like behaviour with a clear bifurcation between the ZFC and FC up to a certain temperature limit was observed. To understand the magnetic behaviour, the inverse susceptibility $(\frac{1}{\chi} \text{ vs T})$ data, as shown in figure 11(b) was plotted. The nature of inverse susceptibility data with respect to temperature is not uniform. It can be observed that two different magnetic transitions in different temperature zones. Considering the low-temperature region, we found a typical ferrimagnetic behaviour that was well fitted with the Neel equation $(\frac{1}{\chi} = \frac{T}{C} + \frac{1}{\chi_0} - \frac{\sigma}{T - \theta})$. The best fit (adj. $R^2 = 0.99$) in the low-temperature region (2– 150 K), as shown in figure 11(b), provides different fitting parameters, such as $C = 3.54 \times 10^{-3}$ emu K g⁻¹ Oe⁻¹, $\chi_0 = 1.24 \times 10^{-5}$ emu g⁻¹ Oe⁻¹, $\sigma = 7.79 \times 10^5$ K g Oe emu⁻¹ and $\theta = 9.5$ K. Although all the magnetic parameters are equivalent to those of the bare-Ti₃C₂T_x MXene sheets, there is an increase in the transition temperature from 3.5 to 9.5 K. A possible reason behind the increase in the transition temperature is the heat treatment during the hydrothermal reaction used to produce the composite sample. It is well known that in the case of antiferromagnetic or ferrimagnetic materials, the Neel (T_N) transition temperature solely depends upon the material particle size [42]. The dependency of the Neel temperature occurs as $T_{\rm N}(D) = T_{\rm N}(\infty)[1-\left(\frac{\xi_0}{D}\right)^{\lambda}]$, where ξ_0 and λ are the correlation lengths at the absolute zero temperature and shift exponent, respectively. $T_N(D)$ and $T_N(\infty)$ are the Neel temperatures of a ferrimagnetic material with a finite

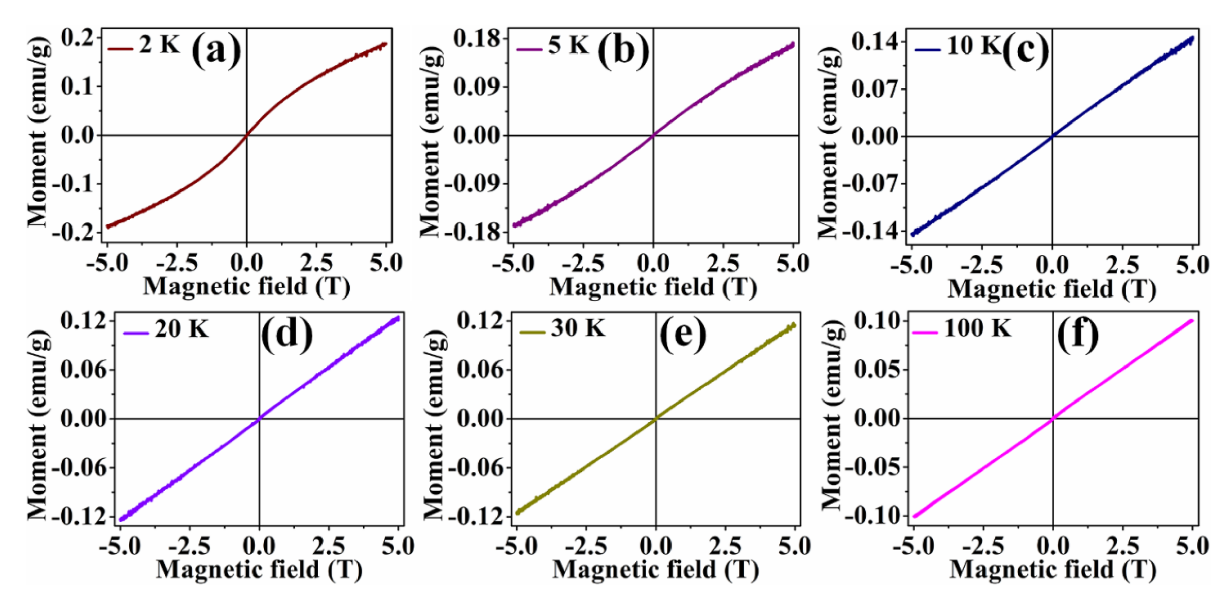


Figure 10. The isothermal magnetization data as a function of magnetic field at temperature of (a) 2 K, (b) 5 K, (c) 10 K, (d) 20 K, (e) 30 K, and (f) 100 K.

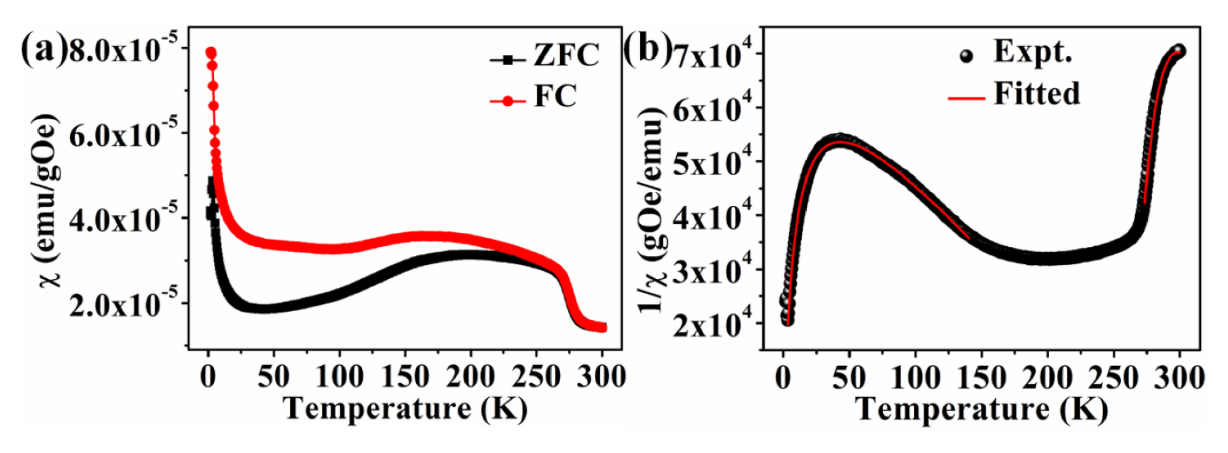


Figure 11. (a) The $\chi(T)$ data in both ZFC and FC mode of β -Ni(OH)₂/Ti₃C₂T_x composite sample. (b) The corresponding inverse susceptibility data fitted with Neel equation.

particle size (D) and bulk dimensions, respectively. During the hydrothermal treatment used to prepare the composite, the particle size of the $Ti_3C_2T_x$ crystal increased, which resulted in a higher Neel transition temperature for the 2D Ti₃C₂T_x MXene sheets than for the bare- $Ti_3C_2T_x$ MXene sheets. The most crucial observation and key point of this study is the 2nd transition in the higher temperature range (>200 K). The best fit (adj. $R^2 = 0.99$), as shown in figure 11(b), provides different fitting parameters, such as $C = 8.10 \times 10^{-3}$ emu K g⁻¹ Oe⁻¹, $\chi_0 = 1.99 \times 10^{-6} \text{ emu g}^{-1} \text{ Oe}^{-1}, \sigma = 3.37 \times 10^6 \text{ K g Oe emu}^{-1}$ and $\theta = 246.2$ K. The value of the Curie constant (C) is relatively greater than that of the bare- $Ti_3C_2T_x$ MXene sheets. The most important thing is the vast increase in the Neel transition temperature. Due to the higher Neel transition temperature, magnetic ordering is expected to occur up to a higher temperature. The isothermal hysteresis curves at different temperatures, as shown in figure 12, reveal ferrimagnetic-like behaviour with a sufficiently high coercivity for the composite sample. The coercivity values at different temperatures are

summarised in table 4. The origin of ferrimagnetic ordering with a sufficiently high transition temperature (>200 K) lies in the charge-transfer phenomenon, commonly referred to as d-p mixing, occurring at the interface of the as-grown antiferromagnetic layer (β -Ni(OH)₂) and the Ti₃C₂T_x sheets. In this study, the Ti₃C₂T_x sheets served as a template for the growth of a thin layer of antiferromagnetic β -Ni(OH)₂. As the β -Ni(OH)₂ layers develop on the surface of the Ti₃C₂T_r sheets, they form an ionic-like bond with negatively charged functional groups (T_x) , such as F [33]. The XPS analysis, detailed in section 3.3, indicates charge transfer from the F p-orbital of $Ti_3C_2T_x$ to the Ni d-orbital of β -Ni(OH)₂. As discussed in the supplementary materials, the charge-transfer effect has also been realised from the density functional theory (DFT) calculation. The DFT calculation shows that there is an influence of the present T_F (of $Ti_3C_2T_x$) functional groups on the density of states (DOS) of the β -Ni(OH)₂, as shown in figure S3 of the supplementary materials. Due to the presence of T_F (of Ti₃C₂T_x) functional groups at the adjacent point of

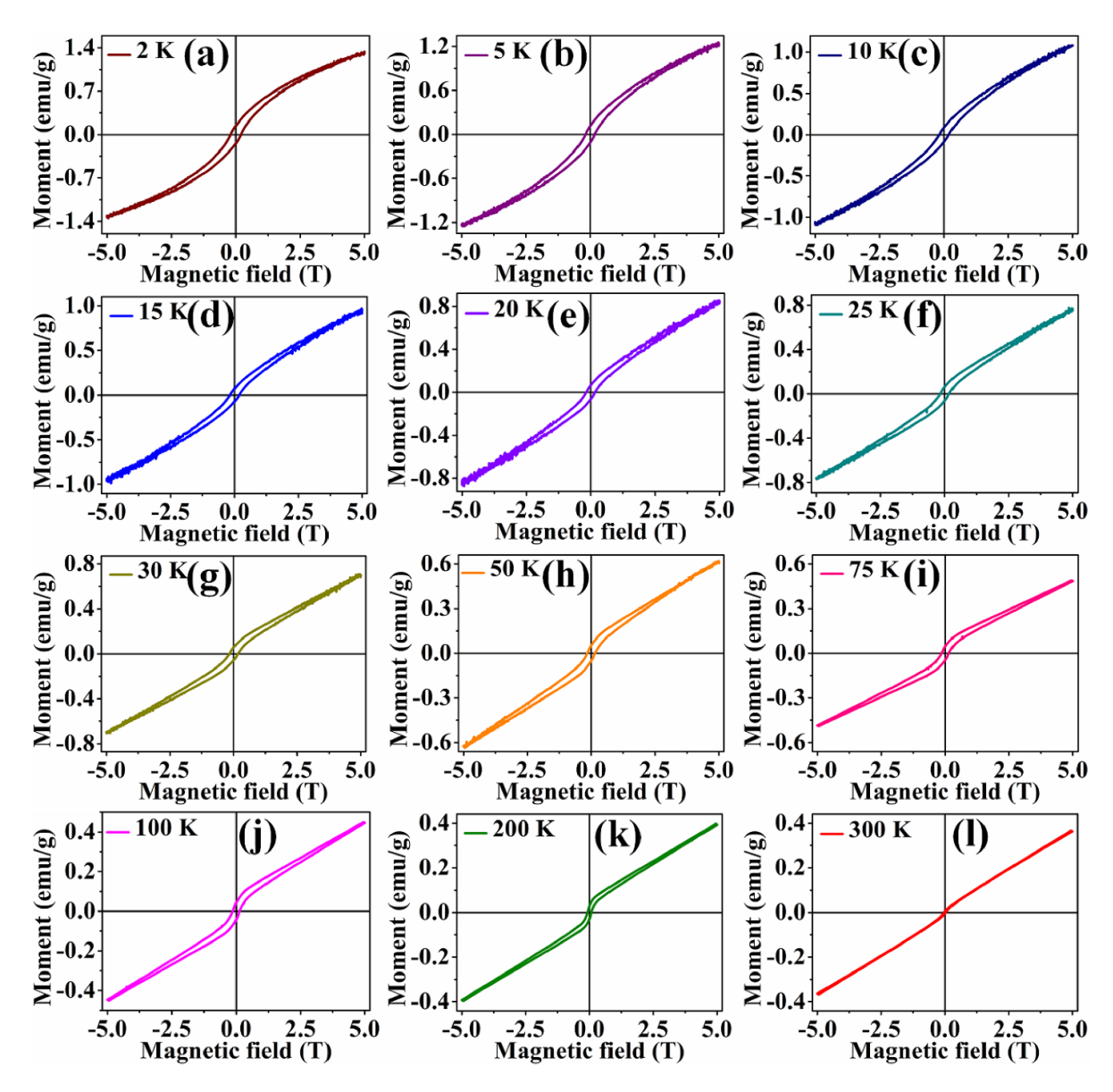


Figure 12. The isothermal magnetization data as a function of magnetic field, for the β -Ni(OH)₂/Ti₃C₂T_x composite sample, at temperatures of (a) 2 K, (b) 5 K, (c) 10 K, (d) 15 K, (e) 20 K, (f) 25 K, (g) 30 K, (h) 50 K, (i) 75 K, (j) 100 K, (k) 200 K, and (l) 300 K.

Ni (of β -Ni(OH)₂), there is a generation of additional electronic states near the Fermi level. This calculation establishes the redistribution of charge within the layers of β -Ni(OH)₂, hence the generation of interfacial magnetic moments. In pristine β -Ni(OH)₂, Ni²⁺ spins are aligned parallelly within a sublattice, whereas the Ni²⁺ spins in other sublattices are aligned antiparallelly [43]. The partial transfer of electrons to the Ni d-orbitals of β -Ni(OH)₂ disrupts the antiferromagnetic nature of the antiparallelly aligned spins within it. This disruption arises from the charge sharing between the F porbital and Ni d-orbital, commonly known as d-p mixing. Consequently, an uncompensated spin moment emerges at the interface of β -Ni(OH)₂ and the Ti₃C₂T_x sheets [19, 20]. The locally generated spin magnetic moments provide magnetic ordering, forming a 2D ferrimagnet at the interface. Remarkably, this ordering persists up to a sufficiently high temperature of approximately 246 K, which is much greater than the actual Neel temperature (\sim 26 K) of the bare β -Ni(OH)₂ crystal. The origin of the high coercivity at different temperatures is the strong surface-pinning effect of spins, usually observed at the interface of two ultrathin magnetic layers [44].

The coercivity values at different temperatures are plotted as a function of temperature in figure 13. The coercivity decreases with increasing temperature according to Kneller's law $(H_C = H_0(1 - \frac{T}{T_0})^{\alpha})$, where H_0 is the coercivity at the absolute zero temperature and α is an exponent [45]. The coercivity at 2 K shows a slight deviation. The coercivity data are consistent with those of conventional ferrimagnetic or ferromagnetic substances. The tendency of the isothermal hysteresis loops at higher temperatures to exhibit non-saturation magnetisation indicates the fractional presence of some antiferromagnetic component within the composite materials.

Table 4. Coercivity values of the β -Ni(OH)₂/Ti₃C₂T_x composite sample at different temperatures.

Temperature	Forward coercivity (T)	Reverse coercivity (T)	Average coercivity (T)
2	0.201	0.199	0.200
5	0.181	0.180	0.180
10	0.179	0.177	0.178
15	0.173	0.171	0.172
20	0.171	0.170	0.170
25	0.165	0.164	0.164
30	0.161	0.160	0.160
50	0.153	0.152	0.152
75	0.138	0.137	0.137
100	0.127	0.126	0.126
200	0.076	0.074	0.075
300	0.029	0.029	0.029

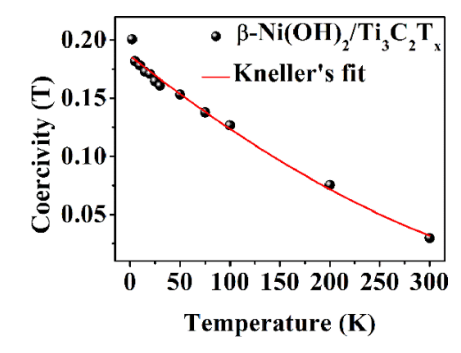


Figure 13. Variation of coercivity with temperature for the β -Ni(OH)₂/Ti₃C₂T_x composite sample.

4. Conclusions

In conclusion, the wet-chemical synthesis process utilising an HF-generating (LiF + HCl) etchant successfully yielded ultrathin 2D Ti₃C₂T_x MXene microsheets through the etching of Al layers from the Ti₃AlC₂ MAX phase. Rietveld refinement analysis of powder XRD data provided a comprehensive understanding of the synthesis mechanism, highlighting the exfoliation of Ti₃C₂T_x MXene layers. Magnetic resonance studies revealed weak ferrimagnetic behaviour with low coercivity value in the resulting 2D Ti₃C₂T_x MXene microsheets. The introduction of ultrathin layers of β -Ni(OH)₂ on to the MXene surface demonstrated the generation of magnetic moments through charge transfer, known as d-p mixing. The charge transfer effect has been realised from the generation of additional electronic states near the Fermi level of the β -Ni(OH)₂ in the presence of the nearby functional groups (T_F) of Ti₃C₂T_x. Hence, the charge redistribution within the β -Ni(OH)₂ indicates a hindrance to the antiferromagnetic properties within it. Consequently, a generation of magnetic moment occurs at the interface of β -Ni(OH)₂ and Ti₃C₂T_x. These charge-transfer-induced magnetic moments exhibit ordering up to a sufficiently high temperature. The composite structure $(\beta-Ni(OH)_2/Ti_3C_2T_x)$ exhibited a notably high coercivity of 0.2 T at 2 K, making it a promising candidate for spintronic devices. Importantly, the ferrimagnetic ordering remained stable at temperatures up to 264 K, indicating practical applicability for diverse technological uses. Overall, the successful synthesis and characterisation of this novel composite $(\beta\text{-Ni}(OH)_2/Ti_3C_2T_x)$ open avenues for further exploration and development of advanced multifunctional materials with tailored magnetic properties.

Data availability statement

All data that support the findings of this study are included within the article and the supplementary file.

Acknowledgments

A D acknowledges the Science and Engineering Research Board (SERB), Government of India, for providing the National Post-Doctoral Fellowship (NPDF) and financial support through the SERB-NPDF programme (File No. PDF/2022/000231). S B and G M acknowledge University Grants Commission (UGC), Government of India. A K acknowledges Council of Scientific & Industrial Research (CSIR), Government of India. A D and S K S acknowledge the Indian Association for the Cultivation of Science (IACS), Kolkata, India, for providing infrastructural and financial support. A D acknowledges the Jadavpur University (JU), Kolkata, India, for providing infrastructural facilities. S K S expresses sincere gratitude to Professor Yan-Kuin Su, Academy of Innovative Semiconductor and Sustainable Manufacturing, National Cheng Kung University, for the valuable discussion during the review of the manuscript.

Conflict of interest

The authors have no conflicts to disclose.

ORCID iDs

Anup Debnath https://orcid.org/0000-0002-7308-9902 Sumanta Bera https://orcid.org/0000-0003-3005-6390 Gouranga Mahapatra https://orcid.org/0009-0002-6820-3827

Shyamal K Saha https://orcid.org/0000-0002-6302-9105

References

- [1] Naguib M, Kurtoglu M, Presser V, Lu J, Niu J, Heon M, Hultman L, Gogotsi Y and Barsoum M W 2011 Adv. Mater. 23 4248–53
- [2] Alhabeb M, Maleski K, Anasori B, Lelyukh P, Clark L, Sin S and Gogotsi Y 2017 Chem. Mater. 29 7633–44
- [3] Gogotsi Y and Anasori B 2019 ACS Nano 13 8491–4
- [4] Long Y, Tao Y, Shang T, Yang H, Sun Z, Chen W and Yang Q H 2022 Adv. Sci. 9 2200296
- [5] Zeraati A S, Mirkhani S A, Sun P, Naguib M, Braun P V and Sundararaj U 2021 Nanoscale 13 3572
- [6] Wang C et al 2019 Adv. Opt. Mater. 7 1900060
- [7] Qiao C, Wu H, Xu X, Guan Z and Yang W O 2021 Adv. Mater. Interfaces 8 2100903

- [8] Hantanasirisakul K, Zhao M Q, Urbankowski P, Halim J, Anasori B, Kota S, Ren C E, Barsoum M W and Gogotsi Y 2016 Adv. Electron. Mater. 2 1600050
- [9] Ahouei M A, Syed T H, Bishop V, Halacoglu S, Wang H and Wei W 2023 Catal. Today 409 162–72
- [10] Lim G P, Soon C F, Ma N L, Morsin M, Nayan N, Ahmad M K and Tee K S 2021 Environ. Res. 201 111592
- [11] Liu P, Yao Z, Ng V M H, Zhoub J, Kong L B and Yue K 2018 Composites A 115 371–82
- [12] Yang F, Yao J, Jin L, Huyan W, Zhou J, Yao Z, Liu P and Tao X 2022 *Composites* A 243 110161
- [13] Kumar H, Frey N C, Dong L, Anasori B, Gogotsi Y and Shenoy V B 2017 ACS Nano 11 7648–55
- [14] Shein I R and Ivanovskii A L 2012 *Comput. Mater. Sci.* **65** 104–14
- [15] Iqbal M, Fatheema J, Noor Q, Rani M, Mumtaz M, Zheng R-K, Khan S A and Rizwan S 2020 Mater. Today Chem. 16 100271
- [16] Scheibe B, Tadyszak K, Jarek M, Michalak N, Kempiński M, Lewandowski M, Peplińska B and Chybczyńska K 2019 Appl. Surf. Sci. 479 216–24
- [17] Yoon Y, Le T A, Tiwari A P, Kim I, Barsoum M W and Lee H 2018 Nanoscale 10 22429
- [18] Debnath A, Bhattacharya S and Saha S K 2017 Phys. Rev. B 96 214433
- [19] Debnath A, Bhattacharya S and Saha S K 2020 J. Phys. D: Appl. Phys. 53 225004
- [20] Debnath A, Bhattacharya S, Mondal T K, Tada H and Saha S K 2020 J. Appl. Phys. 127 013901
- [21] Bhattacharya S, Dinda D, Shaw B K, Dutta S and Saha S K 2016 Phys. Rev. B 93 184403
- [22] Yedluri A K, Kulurumotlakatla D K, Sangaraju S, Obaidat I M and Kim H-J 2020 J. Energy Storage 31 101623
- [23] Rietveld H M 1969 J. Appl. Crystallogr. 2 65
- [24] Lutterotti L, Matthies S and Wenk H R 1999 MAUD (material analysis using diffraction): a user-friendly Java program for Rietveld texture analysis and more *Proc. Twelfth Int. Conf.* on Textures of Materials (ICOTOM-12) (Montreal, Canada) (National Research Council (NRC) Research Press) vol 1 p 1599

- [25] Wang X, Shen X, Gao Y, Wang Z, Yu R and Che L 2015 J. Am. Chem. Soc. 137 2715–21
- [26] Ding L, Wei Y, Li L, Zhang T, Wang H, Xue J, Ding L-X, Wang S, Caro J and Gogotsi Y 2018 Nat. Commun. 9 155
- [27] Sui J, Chen X, Li Y, Peng W, Zhang F and Fan X 2021 RSC Adv. 11 16065
- [28] Shi C, Beidaghi M, Naguib M, Mashtalir O, Gogotsi Y and Billinge S J L 2014 Phys. Rev. Lett. 112 125501
- [29] Jain A et al 2013 APL Mater. 1 011002
- [30] Shuck C E, Sarycheva A, Anayee M, Levitt A, Zhu Y, Uzun S, Balitskiy V, Zahorodna V, Gogotsi O and Gogotsi Y 2020 Adv. Eng. Mater. 22 1901241
- [31] Persson I, Näslund L-Å, Halim J, Barsoum M W, Darakchieva V, Palisaitis J, Rosen J and Persson P O Å 2018 2D Mater. 5 015002
- [32] Mansour A N and Melendres C A 1994 Surf. Sci. Spectra 3 247
- [33] Xie X, Chen C, Zhang N, Tang Z-R, Jiang J and Xu Y-J 2019 Nat. Sustain. 2 856–62
- [34] Park J, Ryu S, Han M-S and Oh S-J 1988 Phys. Rev. B 37 10867
- [35] Pavao A C and Silva J P B D 1989 J. Phys. Chem. Solids 50 669473
- [36] Rosencwaig A, Wertheim G K and Guggenheim H J 1971 Phys. Rev. Lett. 27 479
- [37] Samal R, Mane P, Ratha S, Chakraborty B and Rout C S 2022 Energy Fuels 36 15066–79
- [38] Zuo D C, Song S C, An C S, Tang L B, He Z J and Zheng J C 2019 Nano Energy 62 401–9
- [39] Hall D S, Lockwood D J, Bock C and MacDougall B R 2015 Proc. R. Soc. A 471 20140792
- [40] Yu X, Zhao J, Zheng L R, Tong Y, Zhang M, Xu G, Li C, Ma J and Shi G 2018 ACS Energy Lett. 3 237–44
- [41] Morrish A H 2001 *The Physical Principles of Magnetism* (IEEE Press) pp 492–3
- [42] Thota S, Shim J H and Seehra M S 2013 *J. Appl. Phys.* **114** 214307
- [43] Bhattacharya S, Kumar E M, Thapa R and Saha S K 2017 Appl. Phys. Lett. 110 032404
- [44] Chen Y and Washburn J 1996 Phys. Rev. Lett. 77 4046
- [45] Kneller E F and Luborsky F E 1963 *J. Appl. Phys.* **34** 656–8